G. Alber, *ibid.* **42**, 3018 (1990).
27. P. Ewart and P. Snowdon, *Opt. Lett.* **15**, 1403 (1990).
28. P. Ewart, *Opt. Commun.* **55**, 124 (1985).
29. I. P. Jefferies, A. J. Yates, P. Ewart, in *Coherent Raman Spectroscopy: Applications and New Developments*, E. Castellucci, Ed. (World Scientific, Singapore, in press).
30. B. Yip, P. M. Danehy, R. K. Hanson, *Opt. Lett.* **17**, 751 (1992).
31. Q. Zhang, S. A. Kandel, T. A. W. Wasserman, P. H. Vacarro, *J. Chem. Phys.* **96**, 1640 (1992).
32. C. E. Hamilton, J. L. Kinsey, R. W. Field, *Annu. Rev. Phys. Chem.* **37**, 493 (1986).
33. M. A. Buntine, D. W. Chandler, C. C. Hayden, *J. Chem. Phys.* **97**, 707 (1992).
34. T. J. Butenhoff and E. A. Rohlfing, *ibid.*, p. 1595.
35. We thank the many researchers cited in this article for making their work available to us at early stages. We especially thank P. H. Vacarro for providing us with Fig. 9. This work was supported by the U.S. Department of Energy, Office of Basic Energy Sciences, Division of Chemical Sciences and Office of Industrial Technologies, Division of Advanced Industrial Concepts, and the Gas Research Institute.

From Molecules to Cells: Imaging Soft Samples with the Atomic Force Microscope

M. Radmacher, R. W. Tillmann, M. Fritz, H. E. Gaub*

Since its invention a few years ago, the atomic force microscope has become one of the most widely used near-field microscopes. Surfaces of hard samples are imaged routinely with atomic resolution. Soft samples, however, remain challenging. An overview is presented on the application of atomic force microscopy to organic samples ranging from thin ordered films at molecular resolution to living cells. Fundamental mechanisms of the image formation are discussed, and novel imaging modes are introduced that exploit different aspects of the tip-sample interaction for local measurements of the micromechanical properties of the sample. As examples, images of Langmuir-Blodgett films, which map the local viscoelasticity as well as the friction coefficient, are presented.

Traditional microscopes use waves, such as light or electrons, and suitable imaging optics to create a two-dimensional projection of certain properties (such as the local absorbency) of the object. In near-field microscopes (*1*), a small probe is brought into close proximity to the object and, by guiding the probe over the surface, a three-dimensional relief of the object is obtained that reflects the nature of the local interaction between the probe and the sample. In the most prominent example of such microscopes, the scanning tunneling microscope (STM) (*2*), the probe is guided such that a given tunneling current between probe and the sample remains constant. In the atomic force microscope (AFM) (*3*) (Fig. 1), force fields between the probe and the sample are used to guide the probe over the surface (*4*). The use of forces has proved to be a general approach and has made the scanning probe techniques relevant to a wide range of applications (*5–14*). It also allows imaging of nonconducting materials under various ambient conditions such as physiological buffer solutions, making it a very promising tool for life sciences (*1, 15–22*). The AFM images reflect, in the widest sense, the local mechanical properties of the sample (*14*). In the case of hard samples, the image is dominated by the surface topology and the tip geometry, whereas for soft samples the viscoelastic properties of the sample contribute significantly to the image formation (*23*). As such, the AFM may be most easily described as the instrumental evolution of the tactile sense toward the delicacy and dimensions of individual molecules.

Imaging with the AFM

Although the AFM shares essential features with the profilometer (*24*), an established instrument which measures the surface topology of hard surfaces by scratching it with a stylus, the AFM has, like all near-field microscopes, historically evolved from the STM (*2*). Like the STM, the AFM uses piezo ceramics to position the probe or sample to an accuracy of fractions of atomic diameters (*25*). In the AFM, the probing tip is mounted at the end of a soft cantilever spring, which is normally made by silicon micromanufacturing (*26*). During imaging, suitable electronics are used to guide the tip over the surface such that the bend of the cantilever, which is equivalent to the applied external force, stays constant. Although there are various ways to measure the deflection of the cantilever (*5, 27*), all commercially available instruments do this optically, either by interferometry or with displacement sensors. The resulting image is an isoforce relief of the sample. Although at the first glance one is tempted to assume that the stiffness of the cantilever would limit the applicable force, it turns out that the local forces between tip, sample, and ambient play the dominant role. In general, the long-ranged van der Waals attraction is balanced by the hard-core repulsion between tip and sample. Additional contributions stem from Coulomb interactions (*13, 28*) and from structural forces, such as hydration forces (*29*). When imaged in air, the meniscus force of a wetting water film may dominate the attraction. Because of the different characteristic decay lengths, the local forces can be only partially balanced by retracting the cantilever. Because of the long-range interactions, not only the geometry of the tip at its very end but its shape in the 10-nm scale becomes relevant (*30*). Here a counterintuitive situation emerges, that the sharper the tip is, the lower the minimum force will be. When the technique was introduced, tiny diamond chips glued onto wire springs were used. The sharpest tips are now grown onto the integrated cantilever tips by electron beam deposition (*31*) (see Fig. 1B). Besides the drastically improved aspect ratio, such tips also exhibit a much smaller curvature radius (*32*), reaching values of 10 nm and

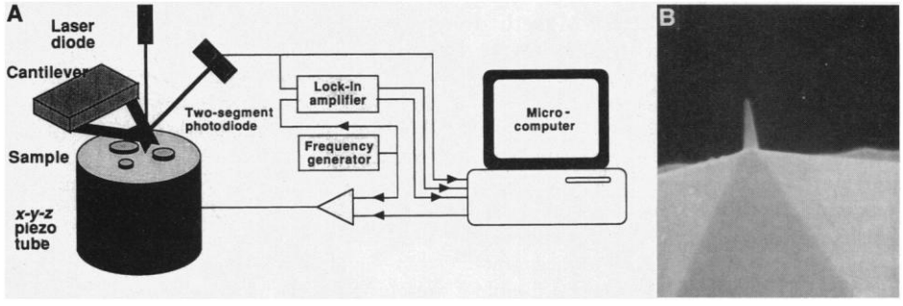

Fig. 1. (**A**) Schematics of an atomic force microscope with a beam bounce deflection sensor. Also outlined are the extensions for viscoelasticity imaging. (**B**) Carbon tip grown on top of the integrated tip of an AFM cantilever (*71*).

The authors are in the Physikdepartment, Technische Universität München, 8046 Garching, Germany.

*To whom correspondence should be addressed.

below, which is especially beneficial when imaging nonflat objects (*18*). Minimum forces obtained with such tips can be as low as fractions of nanonewtons when operated in water and lower when suitable solvents are used (*18, 33*).

Imaging Molecular Crystals, Proteins, and Live Cells

Among the first organic samples that were imaged at molecular resolution were bulk crystals of amino acids (*7, 34*) and crystalline polymers (*35*). Langmuir-Blodgett (LB) type films were soon the object of study with the AFM (*21*) because of their interesting properties and their model aspects for biological membranes. These investigations resulted in the first real-space data of the molecular organization of such films (*17*). Multilayer films readily revealed the packing periodicity of the hydrocarbon chains (see Fig. 2) even when imaged in air (*36–40*) at relatively high forces of several tens of nanonewtons. Thinner films, however, turned out to be quite challenging.

Of great importance for applications in biology is the potential of the AFM to image soft samples in buffer solutions. Supported planar membranes (*41–43*) with bound proteins (*17*) and native membrane fragments of purple membranes (*44, 45*) and gap junctions (*20*) were imaged at molecular resolution. Steady progress was achieved in imaging DNA (*46*), and stable images of plasmids are available now (*18*). Isolated proteins are still hard to image, the difficulty in most cases being their high flexibility (*47*) and their lateral mobility. Actin filaments (see Fig. 3), which are major cytoskeletal elements, (*48*), exhibit just barely enough stiffness to be imaged stably at the resolution of individual monomers of the filament (*22*). During the last year, imaging of live cells has become possible. Here the softness together with the high lateral mobility, or in some cases also the motility, of the cells prevents molecular resolution (see Fig. 4) (*19, 49–51*).

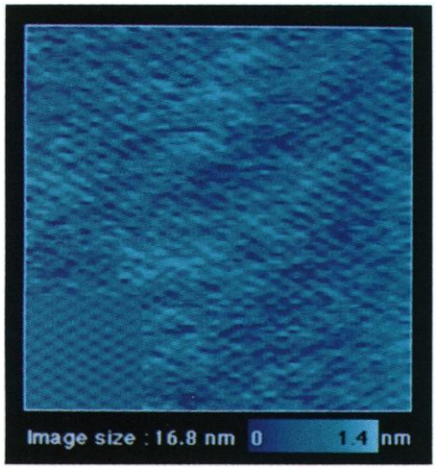

Fig. 2. An AFM image of a Cd-arachidate LB-trilayer on silicon oxide in air. The insert was Fourier-filtered. The unit cell of the lattice has an area of 18.1 ± 2 Å^2 which corresponds to the molecular area of close-packed hydrocarbon chains. The film (*72*) was deposited at 32 mN/m onto a silicon wafer (*57*) following standard procedures (*43*). After the deposition, the sample was stored at room temperature in a desiccator prior to imaging. Imaging parameters: raw data, constant height at ~10 nN, integrated tip, ten lines per second scan speed.

Does the AFM Image Individual Molecules?

On soft samples, the deformability leads to a notable indentation of the sample by the tip. This effect has lead to predictions that the lateral resolution on such samples would be limited to several nanometers (*23, 52*). However, the experimental results of several groups (*36–40, 43*) have demonstrated that organic crystals or ordered molecular films such as LB films may be imaged at molecular resolution. The question still remained whether this resolution was obtained by a point interaction or by the coherent superposition of several signals. In other words, was the periodicity of the lattice reproduced, or were individual molecules imaged? Recent results on multilayer LB films, showing the grain boundary between two single crystals at molecular resolution, strongly suggest that individual molecules may be imaged with the AFM (*53*). The images in Fig. 5 provide an answer to this question for monomolecular films. They show a top view of close packed hydrocarbon chains of a Cd-arachidate monolayer on amorphous silicon oxide. The images in Fig. 5, A and B, were recorded quasi-simultaneously during back and forth scanning while scanning downward, whereas those in Fig. 5, C and D, were recorded while

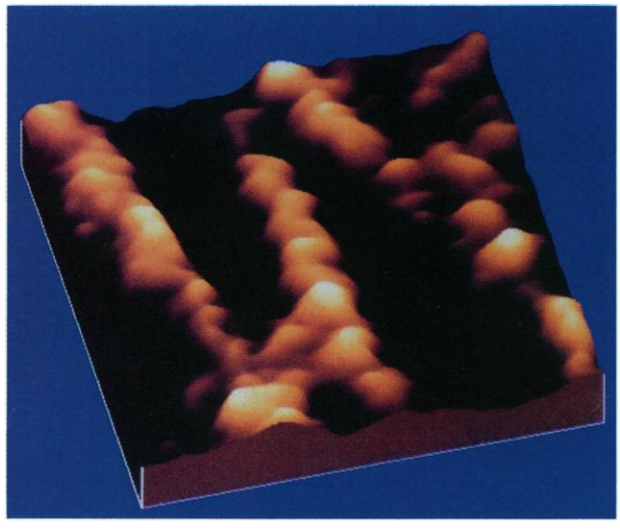

Fig. 3. An AFM image of individual actin filaments in buffer (*22*). Image size is 60 nm. The image is low-pass filtered. The filaments were allowed to self-assemble from a monomer solution at the mica surface just before imaging. For details, see (*22*).

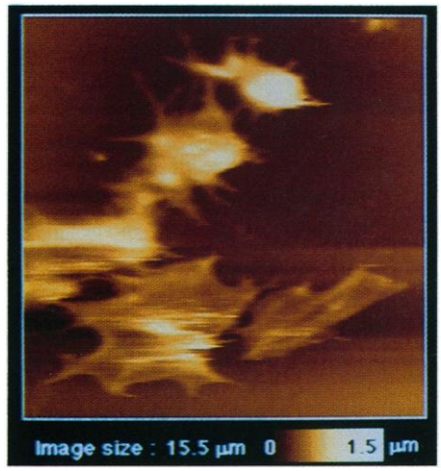

Fig. 4. Live human platelets at different stages of their activation on glass imaged with the AFM. Imaging parameters: raw data, constant force at ~5 nN, carbon tip, five lines per second scan speed. Sample preparation: fresh human platelet concentrate was obtained by the BRK (Bayrisches Rotes Kreuz, München). The platelets were suspended in ACD (acid-citrate-dextrose anticoagulant solution: 18 mM dextrose, 8 mM Na_3-citrate, and 5.2 mM citric acid) and stored for a few hours at room temperature. Ten minutes before the experiment, the platelets were washed in Hepes Tyrode buffer (3 mM Hepes, 4 mM NaH_2PO_4, 137 mM NaCl, 2.6 mM KCl, 1 mM $MgCl_2$, pH 7.3) and centrifuged at 110 g for 10 min at room temperature. The pellet was resuspended in Hepes Tyrode buffer to a final concentration of 10^5 platelets per microliter. The cells were allowed to adhere for 30 s to the coverslip before imaging.

scanning upward (*54*). Although locally the molecules exhibit a tight packing of the chains, which in some places looks like a hexagonal lattice, this film is not well ordered. A more detailed analysis has shown that the autocorrelation function decays at distances beyond the fifth-neighbor molecule. A comparison between the individual scans clearly shows that certain local structures appear to be rather stable. The dark cleft in the lower leftmost corner, for example, appears unaltered in all four scans (*55*). This result clearly demonstrates that under certain conditions the AFM may image individual molecules in organic films, rather than just reproduce their lattice.

This seeming contradiction of the evident molecular resolution and the large contact area between tip and sample may be resolved by two additional assumptions: (i) the tip must exhibit a pronounced micro-roughness on molecular dimensions, which provides a point interaction with individual molecules; and (ii) the repulsive tip-sample interaction must have a strong nonlinear distance dependence with a characteristic decay length that is on the order of the height of the microroughness. Such a repulsion, which may already be inherent in the elastic interaction between tip and sample, would distribute the load over a larger area but would not significantly reduce the contrast (*30*). An additional source of a rapidly decaying repulsion may result from the hydration shell of the tip and, in cases where hydrated surfaces are imaged, also that of the sample. The hydration interaction is known to decay exponentially with a characteristic length of several angstroms (*29, 56*). Evidence for the roughness of the tip was found in studies on hydrated amorphous silicon oxide (*57*).

Imaging Mechanical Properties of Thin Organic Films

All of the given examples show that with increasing softness of the samples the resolution decreases, which indicates that elasticity plays a dominant role in the image formation of soft samples. The sensitivity for the mechanical properties in turn opens a new window for the AFM—imaging mechanical properties. Because LB films offer custom designable mechanical properties (*58*), they were used in the examples below as well-defined model systems for assessing and separating the different contributions to AFM images.

Whenever the effective stiffness of sample and cantilever become comparable, the measured height is also a function of the elasticity of the sample. In the same sense, a variation of the vertical sample position would, through a change of the applied force, result in a measurable change of the indentation (*14*). This effect may be used to measure the local elasticity of the sample with the AFM. The principle of the corresponding experiment is depicted in Fig. 6. As has been pointed out already, the tip geometry is largely unknown at molecular dimensions. However, in the case where the deformation of the sample is large compared to the roughness of the tip, the very end of the tip may be approximated by a sphere with the radius R. If the interaction between tip and surface is dominated by an elastic indentation rather than by an adhesion between tip and sample, the deformation of tip and sample is described by the Hertz model (*59*). Here a force F_n on a tip with radius R leads to an indentation of the depth d in the sample with the elastic modulus E^* according to:

$$d^3 = (9\pi^2/16)\,[F_n^2/(E^{*2}R)] \qquad (1)$$

where $E^* = (\pi E)/(1 - \nu^2)$, ν is the Poisson ratio, and E is the Young's modulus, respectively. It was assumed here that the deformation of the tip is negligible and that the elastic properties of the sample are homogenous and isotropic. If we expand this relation around a typical equilibrium load F_o we obtain the linearized form:

$$\partial F_n/\partial d = K_{eff} = [(6/\pi^2)(E^{*2}R\,F_o)]^{1/3} \qquad (2)$$

With a radius R = 10 nm, an imaging force of F_o = 1 nN, and on a well-ordered LB film with E^* = 9 GPa (*60*), which represents the hardest of the soft samples shown above, the effective stiffness of the tip-sample system K_{eff} turns out to be 7 N/m. This result means that with commercially available cantilevers that have spring constants of fractions of newtons per meter, the elastic constants of soft samples may be measured locally with the AFM.

A laterally resolved map of the mechanical properties is obtained with our instrument by modulating the z-position of the piezo sinusoidally during imaging. Amplitude and phase shift of the tip response are recorded in parallel to the topology. As only the first-harmonic response is measured here, the application of the Hertz model for LB-films is justified.

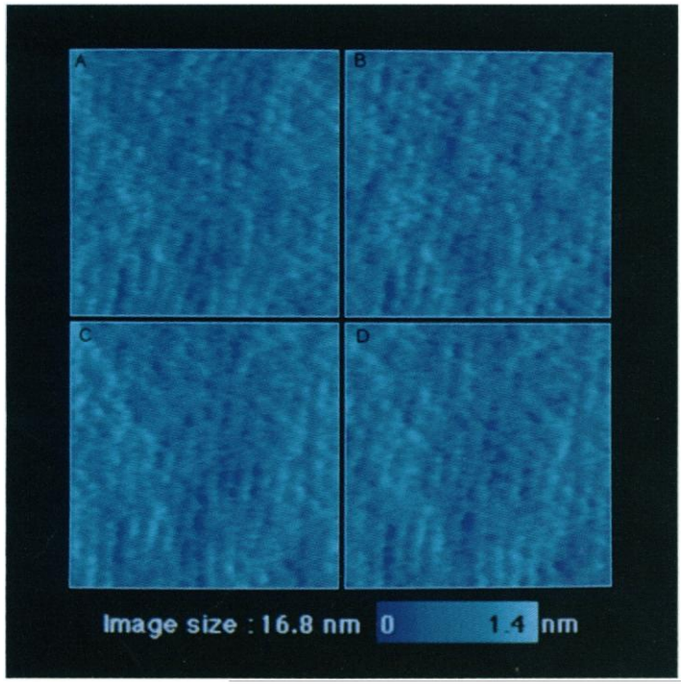

Fig. 5. Monomolecular Cd-arachidate film on silicon oxide imaged in air (raw data). Images (**A**) and (**B**) were recorded line interlaced during (A) forth and (B) back scans while scanning downward, whereas images (**C**) and (**D**) were recorded in the same way scanning upward. Imaging parameters: raw data, constant height at ~3 nN, carbon tip, six lines per second scan speed. For sample preparation, see Fig. 2.

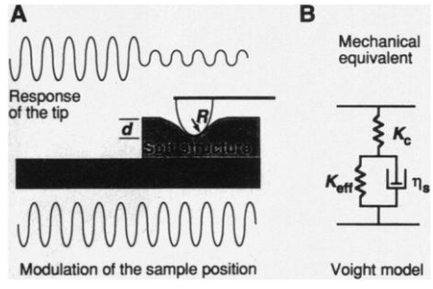

Fig. 6. Schematics of the viscoelasticity measurement with the AFM. (**A**) The modulation of the vertical sample position leads to a modulation of the force between tip and sample. The amplitude of the tip may then be analyzed based on the mechanical equivalent (**B**). The in-phase amplitude of the harmonic response is a function of the elasticity. The viscous element induces a phase shift.

Contributions due to anisotropy and nonlinearity may be measured by detecting the anharmonic modes of the system (*61*). The simplest linear mechanical equivalent model, a three-parameter Voight model, is depicted in Fig. 6B. The cantilever is represented by a spring only. As long as the modulation frequency is below the resonance frequency of the cantilever, its inertia is negligible. Also negligible are the hydrodynamic contributions to the tip-sample interaction in the frequency domain that is relevant here (*62*). All other dissipative contributions besides the one from the sample are constant and may be omitted for the understanding of the image formation. For low viscosities, the in-phase response of the tip position is reduced proportional to the ratio of spring constant of the cantilever and the effective stiffness of the sample. Equation 2 can be used to determine the local elastic modulus of the sample. In addition to the elasticity, the local viscosity is also measurable. The out-of-phase component of the response amplitude is proportional to the loss modulus (*63*). A phase shift of the response is expected when energy is dissipated.

The result of such an experiment is depicted in Fig. 7. It shows the surface profile, the total compliance, and the loss angle recorded for a monomer-polymer LB alloy. This sample is the two-dimensional equivalent of a liquid-crystalline polymer. The high plateaus consist of a well-ordered crystalline polymeric diacetylene film (*43*), whereas the hexagonally shaped imprints consist of monomeric fluid lipid. These microscopic inclusions were built into the film to improve its large-scale mechanical properties in a way similar to plasticizers. In the topology image, the fluid film inclusions appear about 7 ± 1 Å lower than the polymeric matrix. Within experimental errors, this value would also be expected from molecular dimensions of the molecules. The image of the total compliance reveals that these areas are significantly softer, and the image of the loss angle indicates that energy is dissipated in these soft areas. This experiment demonstrates that the local micromechanical properties and topology are measurable simultaneously and separately with an extended AFM. A quantitative analysis is given at the end of the section below.

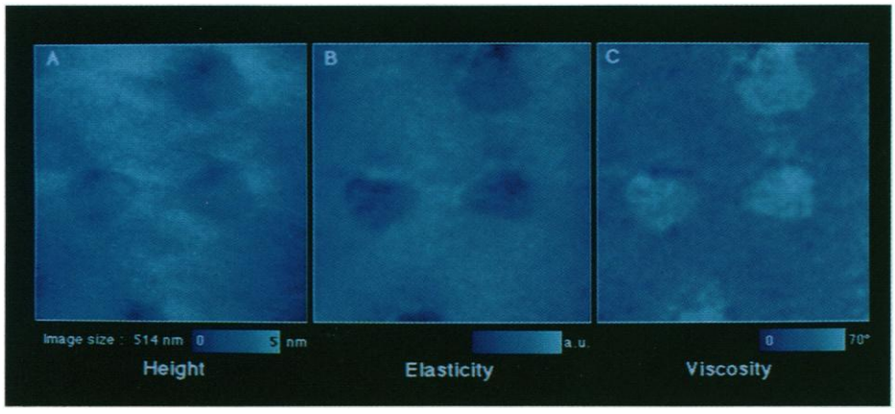

Fig. 7. (**A**) Topology, (**B**) stiffness, and (**C**) viscosity of monomolecular crystalline-polymeric composite LB film with fluid inclusions on silicon oxide. Imaging parameters: raw data, constant height at ~10 nN, integrated tip, 0.5 line per second scan speed, force modulation ~0.5 nN at 12.5 kHz. Sample preparation: A mixture of 70 mol% 10, 12-*N*-2-(2-aminoethoxy)ethyl-10,12-pentacosadiinamide (gift of Biocircuits, Belmont, California) and 30% DMPC (dimyristoylphosphatidylcholine) (*72*) was spread at the air-water interface from an organic solution, compressed to 25 mN/m, and polymerized with ultraviolet light at constant pressure for 1 min before it was transferred by standard LB technique onto a silicon wafer. For details, see (*57*).

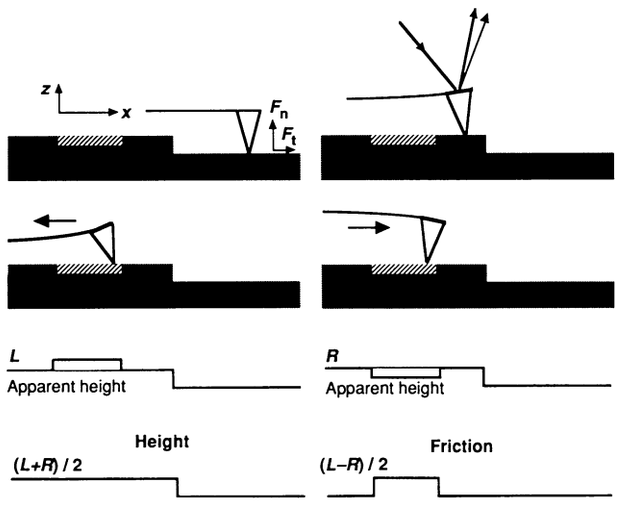

Fig. 8. Schematics of the contribution of friction to the image formation. The topology of the sample is measured through the angle of deflection of a laser beam from the back of the cantilever. Lateral forces also contribute to this deflection through a bend of the cantilever.

Measuring Local Friction with the AFM

The potential use of AFM for friction measurements was recognized quite early by several groups (*64–66*). Instruments were built that measured lateral forces either through the torsion (*67*) of the cantilever or its horizontal bend (*68*) with additional detectors. However, even in standard imaging with the AFM, lateral forces may contribute significantly to the image (*69*) and may, under certain conditions, be separated from the topology through bidirectional scanning (*54*). The schematics of this approach are given in Fig. 8.

In a good approximation, the bend z of the cantilever under load at one end is given by a quadratic relation of the form:

$$z = (F_n/K_c)(x/L)^2 \quad (3)$$

where F_n is the normal force acting between tip and sample at $x = L$ and K_c is the bending stiffness of the cantilever. The deflection of the laser beam is proportional to the tilt of the reflecting mirror at the end of the cantilever and is thus proportional to:

$$dz/dx|_{x=L} = (2F_n/K_c)(x/L^2) = 2z/L \quad (4)$$

which means that the deflection of the laser beam is proportional to the lift at the end of the cantilever L.

A tangential force F_t on the tip of the length h (such as that caused by friction) would result in a bending moment $M = hF_t$, which would result in an additional bend of the cantilever of the form:

$$dz_f/dx|_{x=L} = 2\ h\ F_t/(K_cL^2) \quad (5)$$

This bend also contributes to the laser deflection. Thus the lateral force appears as a pseudoheight z_f, which is given by:

$$z_f = (F_t/K_c)\ (h/L) \quad (6)$$

Therefore, the apparent height z_a, which is measured in the experiment, has two contributions, one from the normal displacement of the tip z and one from the tilt, z_f, so that

$z_a = z + z_f$. Because the lateral force changes its sign during back and forth scanning, both contributions may be separated by subtracting or adding two images that are recorded during back and forth scanning. Under conditions where the friction is small and other nonlinear effects caused by the torsion are negligible, this procedure results in a corrected image of the topology and an additional image of the friction.

An example is given in Fig. 9. It shows a Cd-arachidate monolayer on silicon oxide, which was kept in humid ambient atmosphere. It is known that LB films may, as a function of the ambient, undergo a structural reorganization that results in the local formation of multilayers at the expense of a homogeneous coverage of the substrate. When imaged with the AFM, laterally extended structural features with an apparent height of more than one thousand angstroms were found (Fig. 9A). Upon scanning in the reversed direction, however, certain structures inverted their contrast (Fig. 9B). When the two pseudotopology images were transformed into height and friction images, it became apparent that the height step of the inverting structure corresponded to a monolayer and the step height of the non-inverting struc ture was approximately that of a bilayer. The image of the storage modulus (Fig. 10C), which was recorded in parallel, revealed that the inverting structures were harder than the rest of the surface so that the inverting structure appears to be the bare substrate. In this area, the friction force between tip and substrate is by ~50 nN (see Eq. 6) greater than on the monolayer. The decrease in friction from the monolayer to the trilayer (bilayer on top of the monolayer) is only marginal. These values compare qualitatively well with previous data (68). The high contrast between monolayer and substrate may additionally be caused by a local modulation of the normal force between tip and sample due to the meniscus force of the water film (69). This effect results in a drastic increase of the normal force on silicon oxide, which in turn locally increases the friction on silicon oxide compared to the hydrophobic lipid surface. If this interpretation is correct, it would mean quite generally that the internal forces between tip and sample may modify the apparent height signal in AFM through their contribution to the lateral forces. These findings shed light on speculations that a major contribution to the image contrast even on molecular dimensions may result from lateral forces (70).

Because the stiffness of the silicon oxide substrate is much greater than that of the LB film, the modulation amplitude in the uncovered area could be used in this case to calibrate the modulation on the LB film. The phase shift in this sample was negligible, so that the measured amplitude response is directly proportional to the effective stiffness of the monolayer. The measured K_{eff} was 0.5 N/m. In the absence of published data for monolayers, we have to compare our value with the values measured on multilayers (60). It turns out that this monolayer is about one order of magnitude softer than the multilayer. In view of our finding from Figs. 2 and 5, that

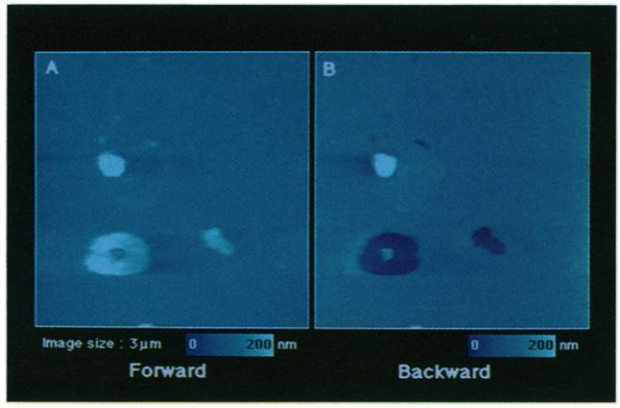

Fig. 9. Pseudoheight images of a Cd-arachidate film in reorganization on silicon oxide recorded while scanning (**A**) forward and (**B**) backward. The horizontal stripes following the structures are a technical artifact and do not represent properties of the sample. Imaging parameters: raw data, constant height at ~10 nN, carbon tip, ten lines per second scan speed. Sample preparation: a monolayer was prepared as described in Fig. 2 but kept in humid ambient atmosphere.

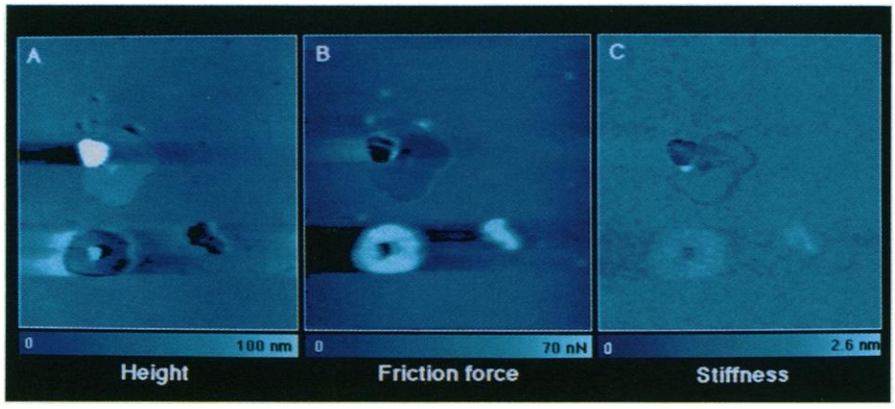

Fig. 10. (**A**) Height, (**B**) friction, and (**C**) stiffness of the film shown in Fig. 9. Images (A) and (B) were calculated from the sum and the difference of Fig. 9, A and B. Additional scan parameters for (C): force modulation ± 0.5 nN at 13 kHz.

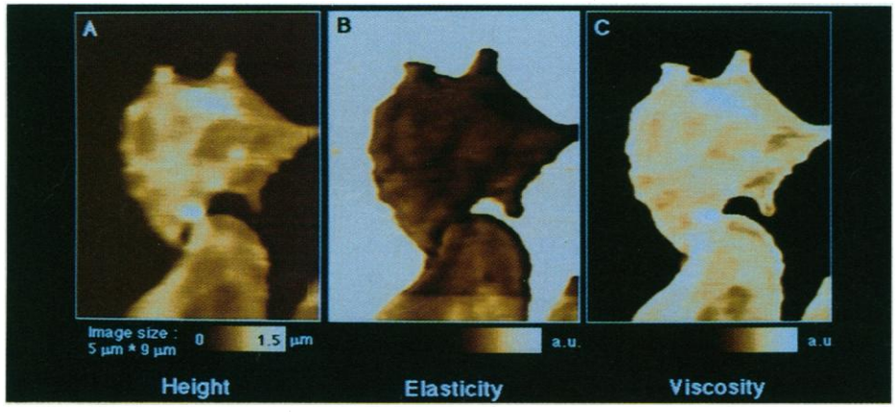

Fig. 11. AFM images of (**A**) height, (**B**) stiffness, and (**C**) viscosity recorded from a live platelet that had undergone full activation just before imaging. Imaging parameters: 5 µm by 9 µm size, raw data, constant force at ~5 nN, integrated tip, 0.5 line per second scan speed, force modulation ± 0.5 nN at 13 kHz for sample preparation, see Fig. 4.

the monolayer is significantly more disordered than the multilayer, the lower elasticity is readily understood. Because the bending stiffness of such films is low, it can also be rationalized that the modulation response of the trilayer is dominated by the soft first layer and thus does not give rise to a significant contrast in the elasticity image. The difference in coupling between the layers of the film and with the substrate becomes apparent in their different boundaries. Where the bilayer on top of the first monolayer exhibits a soft boundary (dark rim in Fig. 10C) of about 100 molecules in width, the first monolayer, which is strongly bound to the substrate by ion bridges, does not show such a rim on that length scale. This soft boundary may be understood by a local melting of the crystalline order at the rim, which in the case of the trilayer is possible because the van der Waals coupling between the layers allows a lateral expansion of the upper bilayer only at the rim in response to the locally applied load.

Outlook

In its classical mode of use, the AFM has proven to be an extremely useful instrument for imaging soft samples down to molecular resolution. The inherent difficulties that arise from the softness of the sample merit more careful analysis, which in turn should give rise to more detailed knowledge about the samples. As such, the AFM is developing more and more into a versatile measuring instrument probing mechanical properties at molecular dimensions. It may gain increasing importance for the investigation of mesoscopic systems in the crossover of molecular and material properties. A richness of novel information is to be expected from the aspects which were dealt with in this article. In Fig. 11 an example is given for further applications where the capability of the AFM is exploited to image elasticity and viscosity of live cells in real time. When well-controlled chemical modifications of the tips allow us to probe and differentiate the complexity and diversity of the local interactions in and on soft systems, even more dramatic improvements of our knowledge on the molecular level can be expected.

REFERENCES AND NOTES

1. P. K. Hansma, V. B. Elings, O. Marti, C. E. Bracker, *Science* **242**, 209 (1988).
2. G. Binnig and H. Rohrer, *Rev. Mod. Phys.* **59**, 615 (1987).
3. G. Binnig, C. F. Quate, C. Gerber, *Phys. Rev. Lett.* **56**, 930 (1986).
4. In the so-called noncontact AFM, which shall not be discussed in detail here, the probe is held in the attractive range of the potential between tip and sample. This approach has the advantage that the technique is largely noninvasive [see (*5*)], but it has not yet been demonstrated to work for samples submerged in liquids [for details, see W. Wiegraebe, M. Nonnenmacher, R. Guckenberger, O. Wolter, *J. Microsc.* **163**, 79 (1991)].
5. H. K. Wickramasinghe, *J. Vac. Sci. Technol.* **A8**, 363 (1990).
6. S. Manne, P. K. Hansma, J. Massie, V. B. Elings, A. A. Gewirth, *Science* **251**, 183 (1991).
7. S. Manne, G. D. Stucky, P. K. Hansma, *J. Cryst. Growth*, in press.
8. C. A. J. Putman *et al.*, *Proc. SPIE* **1639**, 198 (1992).
9. M. Radmacher, M. Fritz-Stephan, H. E. Gaub, *Pure Appl. Chem.*, in press.
10. W. A. Ducker, T. J. Senden, R. M. Pashley, *Nature* **353**, 239 (1991).
11. H. J. Mamin and D. Rugar, *Bull. Am. Phys. Soc. Ser II* **37**, 565 (1992).
12. H. G. Hansma *et al.*, *Langmuir* **7**, 1051 (1991).
13. R. C. Barrett and C. F. Quate, *J. Appl. Phys.* **70**, 2725 (1991).
14. P. Maivald *et al.*, *Nanotechnology* **2**, 103 (1991).
15. A. Engel, *Annu. Rev. Biophys. Biophys. Chem.* **20**, 79 (1991).
16. H. Rohrer, *Ultramicroscopy* **42–44**, 1 (1992).
17. M. Egger *et al.*, *J. Struct. Biol.* **103**, 89 (1990).
18. H. G. Hansma *et al.*, *Science* **256**, 1180 (1992).
19. W. Häberle, J. K. H. Hörber, F. Ohnesorge, D. P. E. Smith, G. Binnig, *Ultramicroscopy* **42–44**, 1161 (1992).
20. J. H. Hoh, R. Lal, S. A. John, J.-P. Revel, M. F. Arnsdorf, *Science* **253**, 1405 (1991).
21. O. Marti *et al.*, *ibid.* **239**, 50 (1988).
22. A. L. Weisenhorn *et al.*, *Biophys. J.* **58**, 1251 (1990).
23. N. A. Burnham, R. J. Colon, H. M. Pollock, *J. Vac. Soc. Technol.* **A9**, 2548 (1991).
24. E. C. Teague, F. E. Scire, S. M. Baker, S. W. Jensen, *Wear* **83**, 1 (1982).
25. G. Binnig and D. P. E. Smith, *Rev. Sci. Instrum.* **57**, 1688 (1986).
26. S. Akamine, R. C. Barrett, C. F. Quate, *Appl. Phys. Lett.* **57**, 316 (1990).
27. N. M. Amer and G. Meyer, *Bull. Am. Phys. Soc.* **33**, 319 (1988).
28. H. G. Butt, *Biophys. J.* **60**, 777 (1991).
29. J. N. Israelachvili and R. M. Pashley, *Nature* **306**, 249 (1983).
30. M. Radmacher, R. M. Zimmermann, H. E. Gaub, in *The Structure and Conformation of Amphiphilic Membranes*, R. Lipowski, D. Richter, K. Kremer, Eds. (Springer, Berlin, 1992), vol. 66, pp. 24–29.
31. T. Fujii *et al.*, *J. Vac. Sci. Technol.* **B9**, 666 (1991).
32. D. Keller and C. Chih-Chung, *Surf. Sci* **268**, 333 (1992).
33. N. Hartmann, *Phys. Rev. B* **43**, 2404 (1991).
34. B. Drake *et al.*, *Science* **243**, 1586 (1989).
35. S. N. Maganov, *Ultramicroscopy*, in press.
36. E. Meyer *et al.*, *Nature* **349**, 398 (1991).
37. L. Bordieu, P. Silberzan, D. Chatenay, *Phys. Rev. Lett.* **67**, 2029 (1991).
38. H. Yamada, S. Akamine, C. F. Quate, *Ultramicroscopy* **42–44**, 1037 (1992).
39. T. Fujii, T. Okane, S. Arisawa, R. Yamamoto, *STM 91, Abstracts* 266 (1991).
40. C. A. J. Putman, H. G. Hansma, H. E. Gaub, J. Greve, P. K. Hansma, *Langmuir*, in press.
41. A. Weisenhorn *et al.*, *ibid.* **7**, 8 (1991).
42. M. Radmacher *et al.*, in *Scanned Probe Microscopies*, K, Wickramasinghe and F. A. McDonald, Eds. (American Institute of Physics, New York, 1991), vol. 241, pp. 144–153.
43. B. M. Goettgens, R. W. Tillmann, M. Radmacher, H. E. Gaub, *Langmuir* **8**, 1768 (1992).
44. D. L. Worcester, R. G. Miller, P. J. Bryant, *J. Microsc.* **152** (1988).
45. H. J. Butt, K. H. Downing, P. K. Hansma, *Biophys. J.* **58**, 1473 (1990).
46. S. M. Lindsay *et al.*, *ibid.* **61**, 1570 (1992).
47. H. Frauenfelder, F. Parak, R. D. Young, *Annu. Rev. Biophys. Biophys. Chem.* **17**, 451 (1988).
48. O. Müller, H. E. Gaub, M. Bärmann, E. Sackmann, *Macromolecules* **24**, 3111 (1991).
49. M. Fritz, M. Radmacher, H. E. Gaub, unpublished results.
50. E. Henderson, P. G. Haydon, D. S. Sakaguchi, *Science* **257**, 1944 (1992).
51. D. Keller, L. Chang, K. Luo, S. Singh, M. Yorgancioglu, *Proc. SPIE* **1639**, 91 (1992).
52. T. P. Weihs, Z. Nawaz, S. P. Jarvis, J. B. Pethica, *Appl. Phys. Lett.* **59**, 3536 (1991).
53. G. Garnaes, D. K. Schwartz, R. Viswanathan, J. A. N. Zasadzinski, *Nature* **257**, 508 (1992).
54. M. Radmacher, K. Eberle, H. E. Gaub, *Ultramicroscopy* **42–44**, 968 (1992).
55. A comparison of Fig. 5 with Fig. 2 supports the interpretation of diffraction data that the first layer is less well ordered than subsequent layers layers [S. Garoff, H. W. Deckmann, J. H. Dunsmuir, M. S. Alvarez, *J. Phys.* **47**, 701 (1986); D. A. Outka, J. Stöhr, J. P. Rabe, J. D. Swalen, H. H. Rothermund, *Phys. Rev. Lett.* **59**, 1321 (1987)]. Whether this vertical gradient of order is due to crossing over from three to two dimensions or whether it is caused by surface properties of the substrate remains open. Recent STM results with monomolecular adsorbate films, however, make the latter mechanism more likely [J. P. Rabe and S. Buchholz, *Science* **253**, 424 (1991)].
56. R. P. Rand and V. A. Parsegian, *Biochem. Biophys. Acta* **988**, 351 (1989).
57. R. W. Tillmann, M. Radmacher, H. E. Gaub, *Appl. Phys. Lett.* **60**, 3111 (1992).
58. J. D. Swalen *et al.*, *Langmuir* **3**, 932 (1987).
59. K. L. Johnson, K. Kendall, A. D. Roberts, *Proc. R. Soc. London Ser. A* **324**, 301 (1971).
60. R. Zanoni, C. Naselli, J. Bell, G. I. Stegeman, C. T. Seaton, *Phys. Rev. Lett.* **57**, 2838 (1986).
61. M. Radmacher, R. W. Tillmann, H. E. Gaub, unpublished results.
62. J. Rädler and E. Sackmann, *Langmuir* **8**, 848 (1992).
63. N. W. Tschoegl, *The Phenomenological Theory of Linear Viscoelastic Behaviour* (Springer, Berlin, 1989).
64. R. Erlandsson, G. Hadziioannou, C. M. Mate, G. M. McClelland, S. Chiang, *J. Chem. Phys.* **89**, 5190 (1988).
65. A. J. den Boef, *Rev. Sci. Instrum.* **62**, 88 (1991).
66. E. Meyer *et al.*, *Thin Solid Films* **181**, 527 (1989).
67. D. R. Baselt and J. D. Baldeschwieler, *J. Vac. Sci. Technol.*, in press.
68. G. S. Blackmann, C. M. Mate, M. R. Philpott, *Vacuum* **41**, 1283 (1990).
69. T. Thundat *et al.*, *J. Vac. Sci. Technol.* **A10**, 630 (1992).
70. G. Binnig, personal communication.
71. This SEM image is a courtesy of D. Keller.
72. All chemicals unless otherwise indicated were from Sigma (Deisenhofen, Germany).

73. Supported by the Deutsche Forschungsgemeinschaft. We are in debt to P. Hansma for fruitful discussions and to D. Keller for the carbon tips.